

Optimising a Neutron Star Extreme Matter Observatory

Mallika Sinha

Supervisors: Ling Sun, Bram Slagmolen

October 16, 2022

Abstract

Neutron stars, formed from the collapse of massive stars, are the densest known celestial bodies in the observable Universe. The physics that governs neutron stars is extreme and elusive, but can be probed by investigating the gravitational waves emitted by remnant objects formed after the collision of two neutron stars. The Neutron Star Extreme Matter Observatory (NEMO) is a gravitational-wave detector proposed and optimised to investigate post-merger physics of binary neutron star systems. In this paper, we develop a method to calculate the detection rate of binary neutron star post-merger signals for a given a detector configuration. Using the numerical waveforms and modelled detector sensitivity curves, signal-to-noise ratios can be calculated and used to determine what systems would produce a detectable signal in a certain detector configuration. The detection rate can thus be informed by assuming a population of binary neutron star systems. This study will inform future work on optimising the efficiency of NEMO to probe nuclear physics with merging neutron stars.

1 Introduction

Gravitational waves propagate through space-time at the speed of light as oscillations of the gravitational field [1]. Unlike electromagnetic waves, gravitational waves only have weak interactions with matter and can travel vastly unaffected by the medium between the detector and the source [1]. Extremely massive accelerating bodies impart large amounts of energy into space-time, creating such waves that can be observed by gravitational-wave detectors—the first being detected by the Advanced Laser Interferometer Gravitational-Wave Observatory (Advanced LIGO) in 2015 [2, 3]. The Advanced LIGO detectors, in its first observing run (O1), detected three binary black hole (BBH) mergers. In the second observing run (O2), joined partway through by Advanced VIRGO [4], seven BBH mergers and the first binary neutron star (BNS) coalescence were observed [5]. The first half of the third observing run (O3) observed 39 gravitational-wave candidates, including more BNS inspirals, BBH mergers and the first detections of neutron star black hole (NSBH) mergers [6]. The second half of O3, joined by the KAGRA detector [7], adds 35 candidates to the list, spanning similar types of mergers to the first half [8].

Two binary neutron star inspirals have been detected by the current generation of gravitational wave detectors. The first is GW170817 detected in O2 [9], and the second is GW190425 detected in the first half of O3 [10]. The gravitational-wave frequency of a BNS system increases as the orbital radius of the system decreases. At the final stage before collision, the signal gets into the sensitive frequency band of the ground-based detectors and hence can be observed. Properties of the system are estimated by identifying the waveform predicted in General Relativity that best fits the observational data. This gives estimates for parameters like the system mass, mass ratio of the two progenitor stars, radiated energy, etc., to a fairly accurate degree [9]. An important property of the event is the sky location; knowing the location allows for multi-messenger astronomy to take place [11]. GW170817, at the time of detection, was the most precisely localised gravitational-wave signal and allowed for electromagnetic observations across the spectrum. Fermi-GBM and INTEGRAL detected a γ -ray burst signal, GRB 170817A, in an overlapping sky region 1.7 s after the merger event; this placed constraints on the physics of gravity and created the first definitive link between γ -ray bursts and mergers [11]. Electromagnetic follow-up campaigns for this event observed signals from radio, infra-red, optical, ultra-violet, and X-ray, and confirmed the host galaxy for this event, NGC 4993 [11]. The joint gravitational and electromagnetic information provides valuable information about physics and cosmology. For example, the distance to the system inferred from the gravitational-wave signal and the redshift measured using the electromagnetic data are combined to measure the Hubble constant [12].

BNS merger signals have proven to contribute valuable information to neutron star physics. Neutron star properties like the mass, tidal deformability, radius, and spin are all influenced by the structure of the neutron star [13, 14]. The structure of these stars, e.g., the neutron superfluids, the neutron-rich crusts, etc., will likely never be directly observed, but they can be inferred from the star’s properties, which can be studied from

the gravitational-wave signals. The population of merging BNS systems inferred from the first three observing runs is estimated to be $105.5^{+190.2}_{-83.9} \text{ Gpc}^{-3}\text{yr}^{-1}$ [15]. More valuable information, e.g., studies of gravity, cosmology and the as of yet unknown neutron star equation of state (EOS), is expected to be gained with the more sensitive detectors and the increasing detection rate in the future. A key avenue to study neutron star physics is to detect the remnants of the BNS mergers. There are four major scenarios to form the post-merger remnant: prompt formation of a black hole, a hypermassive neutron star that collapses to a black hole within about a second, a supermassive neutron star that collapses to a black hole on a longer time scale, and a stable neutron star [16]. The lifetime of the remnant depends heavily on the properties of the initial binary system and the neutron star EOS. Matching the post-merger gravitational-wave signals predicted under the assumption of various choices of EOS with the observational data can constrain the possible EOS. While there is no current strong evidence of post-merger signals being detected, post-merger gravitational waves emitted from the remnant are possible to be observed in the band of ground-based detectors [16–18]. Gravitational-waves from these remnants are expected to have high frequencies and short damping times and thus lie in ranges where current detectors are insensitive [19].

The Neutron Star Extreme Matter Observatory (NEMO) is a proposed gravitational-wave detector that is dedicated to studying the physics that governs the extremely dense matter in neutron stars. NEMO aims to detect the BNS post-merger signals that occur in the kilohertz range [19]. The detection rate of the post-merger gravitational-wave signals with existing detectors is only between one per decade and one per century [19]. Although the detection rate will increase greatly with the next generation of detectors, e.g., Cosmic Explorer [20] and the Einstein Telescope [21], it will likely take decades to build these detectors and to start observing with them. NEMO aims to supplement the current generation, as a pathfinder for next-generation detectors, and increase the average BNS post-merger detection rate to be around one per year¹ [19]. This would allow for sooner observations of post-merger signals and inform astrophysics that would otherwise only occur decades into the future.

To extract as much physics as possible using NEMO, it is important to evaluate the detection rate for a given detector design or configuration and optimize NEMO to the maximum possible detection efficiency. This study aims to quantify the efficiency of the proposed NEMO detector under various configurations. The structure of the paper is as follows. In Section 2, we explore the physics of the post-merger signals and discuss the detector sensitivity. In Section 3, we detail the method and describe the structure of the analysis pipeline that evaluates the detection rate for any given detector configuration. Section 4 presents the final results. And we provide a conclusion in Section 5.

¹Ref. [19] assumes a binary neutron star merger rate of $250\text{--}2810 \text{ Gpc}^{-3}\text{yr}^{-1}$ [10], which is higher than the updated merger rate of $105.5^{+190.2}_{-83.9} \text{ Gpc}^{-3}\text{yr}^{-1}$ adopted in the analysis of this paper [15].

2 Probe post-merger physics of binary neutron stars

2.1 Post-merger signals

Electromagnetic observations of neutron stars through their X-ray and radio emissions have provided astrophysical constraints on the neutron star mass and radius, e.g., see [22, 23], and thus informed the constraints on the neutron star EOS. However, these observations and constraints cannot provide a comprehensive picture of the neutron star EOS. Electromagnetic observations of neutron stars generally probe stars that have spent sufficient time to cool since their formation. These observations thus investigate the EOS in the cold regime [23]. Gravitational waves, in particular the waves emitted from the post-merger remnants of BNS coalescences, probe neutron stars under fluctuating conditions that involve higher temperatures and densities. This allows us to probe the EOS in the hot and dense regimes, providing a more complete investigation into the EOS.

Studying gravitational waves emitted during different phases of the BNS coalescence is equivalent to investigating neutron stars under different conditions and can thus probe different properties and EOS regimes. The inspiral phase does not induce a large temperature change in the neutron stars, leaving the internal structure vastly unchanged. The gravitational-wave signals from this phase probe a similar cold EOS regime to the electromagnetic observations. The late inspiral sees the rise of tidal effects as the stars draw closer, allowing for more investigation into properties such as the tidal deformability [19]. Such signals occur in the high-frequency band where NEMO aims to be sensitive. The conditions during the merger and post-merger phases contrast greatly with that of the inspiral. Here, temperatures can rise on the order of 100–1000 K, affecting the internal structure and state of the stars greatly [14, 19]. The remnant is in a particularly high-energy state due to the extreme compaction of the system and also has a higher density than the progenitor stars [19]. These extremely hot and dense conditions are predicted to induce phase changes in the matter making up the system [19, 24]. Observations of these phases allow us to probe the hot, dense and energetic regimes of the neutron star EOS. NEMO is proposed to detect these post-merger signals and aims to achieve good sensitivity in the frequency bands these signals occur in.

Gravitational-wave signals are identified using template waveforms. These template waveforms depend on the properties of the system, which are then constrained by comparing the data to the predicted waveforms using analysis techniques such as Bayesian analysis [25]. This study uses a range of numerical waveforms to model the predicted gravitational-wave post-merger signal from a BNS merger event using different neutron star properties, e.g., EOS, mass, etc. Different properties lead to different waveforms with different amplitudes and signal frequencies. In particular, this study focuses on the neutron star EOS, system mass, and the resulting peak frequency of each waveform in order to evaluate the detectability for various systems. In this report the peak frequency indicates the frequency at which the amplitude of the frequency domain strain is at a maximum.

All these three properties of the numerical waveforms are shown in Figure 1. The x -axis shows the total mass of the system and the y -axis shows the peak frequency of the signal. Different EOSs are marked by different colours, as shown in the legend. Most of the post-merger signal peak frequencies occur between 1 kHz and 4 kHz. The ones above 4 kHz are out of the sensitive band of the NEMO detector. Figure 2 shows a histogram of the peak frequencies of the waveforms, indicating that the 2–4 kHz range is particularly important. The EOS can have significant influence on the peak frequency. As shown in Figure 1, fixing the mass at approximately $2.7 M_{\odot}$ gives a frequency range of 0.1–10 kHz. The peak frequencies occurring close to 0 kHz should be investigated in order to determine the accuracy and the usefulness of the model. Extremely low peak frequencies might indicate a model it is not useful to optimise for. This study includes all the waveforms shown in Figure 1, but this can be changed in the future. It is evident that certain EOSs, e.g., the DD2, give much higher frequencies compared to the majority within the 1–4-kHz grey band. We keep these waveforms in this study as they are physically allowed, although lying out of the sensitive band of NEMO.

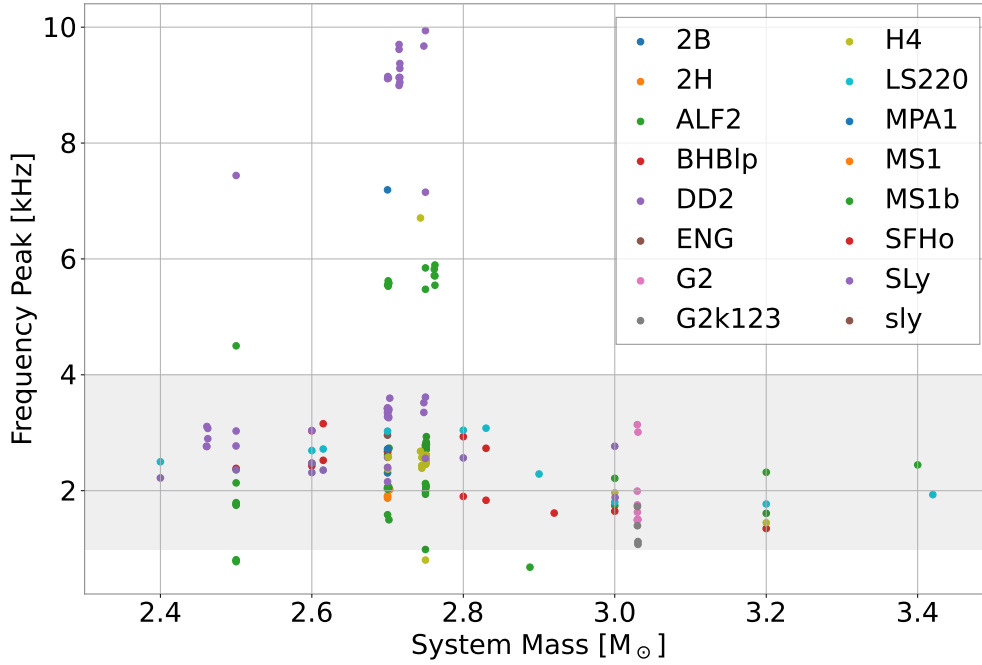


Figure 1: Peak frequency of the numerical waveforms modelled using different neutron star EOSs and masses. The peak frequency of the system occurs at the merger and decreases from there. The x -axis shows the total mass of the two progenitor neutron stars in M_{\odot} and the y -axis shows the peak frequency in kHz. The grey band marks the 1–4 kHz range where most of the peak frequencies occur. The EOSs for the waveforms are listed in the legend.

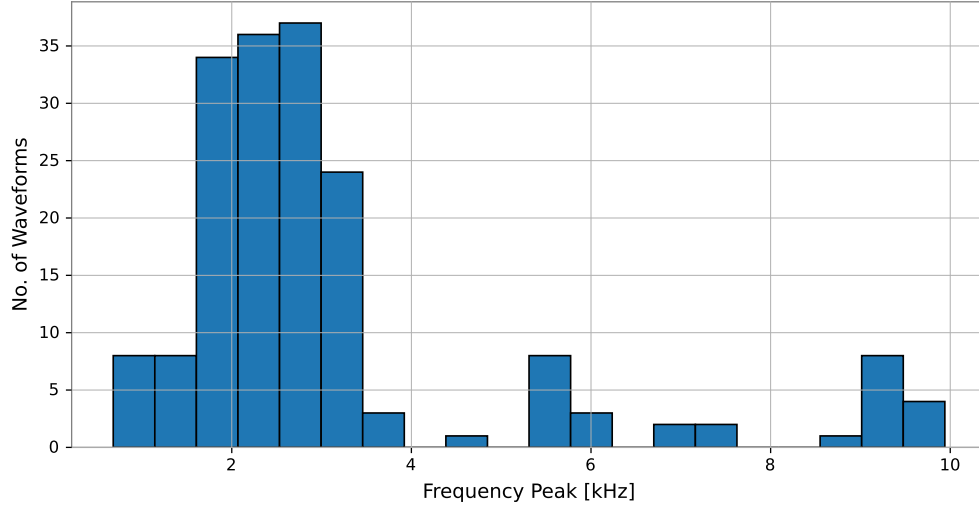


Figure 2: Histogram of peak frequencies of the numerical waveforms. The x -axis shows the peak frequency in kHz and the y -axis shows the number of waveforms that fall in each bin. The histogram has 15 bins in the range of 0–5 kHz, with a total of 179 waveforms. Most of the waveforms have a peak frequency in the range of 1–4 kHz.

The variety of EOSs shown in Figure 1 are all considered in this study. The neutron star EOS considers the nature of strong reactions in nuclear physics. There are three main avenues the EOS explores this: using non-relativistic potential, relativistic field theoretical, or relativistic Brueckner-Hartree-Fock (BHF) physics. Each of these models can include only normal nuclear matter or contain hyperons, pion and kaon condensates, and quarks [26]. The mass-radius relationship described by an EOS is a key characteristic that can be used to compare different EOSs to each other and to astrophysical expected values. For example, the maximum mass described by the EOS, M_{max} , can be compared to the masses of observed NSs. Currently, the heaviest observed NS is the pulsar PSR J0740+6620, weighing approximately $2.072M_{\odot}$ [27].

EOS	M_{max}	References
MS1b	2.776	[28–30]
SLy	2.049	[29–31]
H4	2.032	[29, 30, 32]
ALF2	2.086	[29, 30, 33]
LS220	2.05	[34, 35]
BHB1p	2.10	[35, 36]
DD2	2.42	[34, 35]
SFHo	2.06	[34, 35]
G2	2.09	[32]
MS1	2.767	[28–30]
2B	1.78	[37]
2H	2.83	[37]
ENG	2.240	[29, 30, 38]
MPA1	2.461	[29, 30, 39]

Table 1: Comparison of M_{max} , the maximum non-rotating mass achieved by the EOS with units M_{\odot} , for the EOSs used to simulate the waveforms. EOSs with higher values of M_{max} are often termed ‘stiff’, while EOSs with lower values are often termed ‘soft’.

2.2 Detector Sensitivity

Gravitational-wave detectors are laser interferometers that measure the fringe variation due to the change in the local space-time of the detector caused by gravitational waves [2, 4, 7]. Physical attributes of such detectors include characteristics like the arm cavity length, laser power, mirror properties, etc. These attributes uniquely determine the frequency-dependent amplitude spectral density (ASD) of the detector, and hence the detector’s sensitivity to gravitational-wave signals at different frequencies. These curve generally involves frequency bands of high sensitivity (low ASD) and bands of low sensitivity (high ASD). This constraints the ability of the detector to detect certain signals depending on the frequency of the signal as well as the overall amplitude/power. Even if a detector is sensitive in a similar frequency band to the wave, it cannot detect it reliably if the power of the wave is lower than a certain threshold determined by the curve. It is important to note that some configurations are physically impossible and so not all sensitivity curves are realisable.

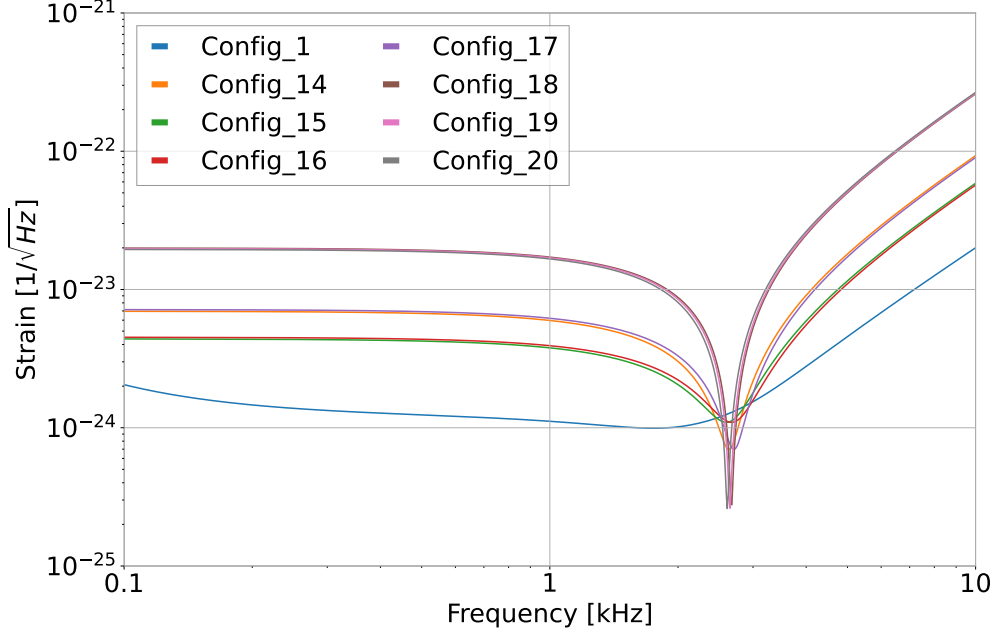


Figure 3: The ASD curves for a selection of different detector configurations. The sensitivity curve of a detector configuration is determined by its physical attributes; different detector configurations can thus provide different sensitivity curves depending on these attributes. Config_1 (blue) is the standard NEMO curve. The signal-to-noise ratio, defined in Eqns. (1) and (2), depends heavily on the power of the signal around its peak frequency and the detector sensitivity in that corresponding frequency band.

Examples of NEMO ASD curves with a few different configurations are shown in Fig 3. These ASD curves, which indicate the detector’s noise floor, can be used to calculate the predicted signal-to-noise ratio (SNR) for a given signal waveform; indicating the likelihood of such a signal to be observed when passing through the detector. When analyzing observational data to detect gravitational waves, the data are parsed through using different template waveforms and statistical techniques. Each of those different types of searches computes a detection-statistic value, evaluates the likelihood of the signal being astrophysical, and the false alarm probability that the noise from the detector would mimic signals with an equivalent or larger detection-statistic value [9]. Depending on the statistical significance of these values, the event is considered to be genuine or contaminated by detector noise. If the SNR is above a certain threshold value, the signal is deemed detectable. NEMO configurations with the most sensitive range lying around 1–4 kHz is favoured because in most of the scenarios, the post-merger signal power is concentrated in this frequency range (see Figure 1).

There are various definitions of SNR given a detector ASD curve and the signal waveform. Two definitions considered here are the optimal SNR, ρ_{opt} , and the matched-filter SNR, ρ_{mf} . The optimal SNR is given by [40]:

$$\rho_{\text{opt}} = \sqrt{\langle h, h \rangle}, \quad (1)$$

and the matched filter SNR is given by [41]:

$$\rho_{\text{mf}} = \frac{\langle x, h \rangle}{\sqrt{\langle h, h \rangle}}, \quad (2)$$

where h is the signal, in this case the numerical waveforms, x is the strain time series (with a signal h present in noise), and $\langle a, b \rangle$ is defined to be:

$$\langle a, b \rangle = 4 \operatorname{Re} \int_0^\infty \frac{\tilde{a}(f) \tilde{b}^*(f)}{S_h(f)} df. \quad (3)$$

Here, $*$ denotes the complex conjugate, $\tilde{}$ denotes the Fourier transform, f indicates the frequency, and $S_h(f)$ the noise power spectral density. This study uses the optimal SNR, ρ_{opt} , and the detection threshold is set to $\rho_{\text{opt}} = 5$.

3 Method

An efficient NEMO will maximise the number of detections of BNS post-merger signals. In order to find the most efficient configuration, it is thus necessary to compare the predicted number of detections with different configurations. We calculate the detection rate for a given detector configuration by taking into consideration a population of BNS mergers. This detection rate, denoted by α , corresponds to the number of BNS post-merger signals occurring in a year with SNR above the threshold value. We can model α using the numerical signal waveforms and modelled detector sensitivities.

It is important to note that the merging BNS do not all have equivalent mass and do not merge at similar distances away from the detector. It is thus important to consider the mass and distance distributions of such systems and reflect these distributions in the simulated population to calculate the SNR using the signal waveforms. The masses of the neutron stars in the BNS are intrinsic elements of the numerical waveform, while the distance of the system is extrinsic. The gravitational-wave strain at the detector scales linearly with distance, and so does the SNR. The relation between the optimal SNR ρ_{opt} at distance d and the optimal SNR at a fiducial distance D , $\rho_{\text{opt},D}$ is then given by

$$\rho_{\text{opt}} = \frac{D \rho_{\text{opt},D}}{d}. \quad (4)$$

While different waveforms need to be used in order to represent different neutron star masses and EOSs, the same waveform can be simply rescaled for systems at different distances.

Given a detector configuration, we calculate the optimal SNR [Eq. (1)] when a particular signal is present, which is referred to as “injecting a signal” to the detector. We calculate the detection rate in three steps. First, we find the waveforms that match the

assumed mass distribution of BNS systems (Section 3.1). This is irrespective of the detector configuration and does not need to be repeated when testing different configurations. Second, we “inject” signals using these waveforms by assuming a fiducial distance, and calculate the fiducial optimal SNR (Section 3.2). At last, to account for the distribution of these systems in the Universe, we recalculate the SNRs by scaling the distance of each injection based on assumed BNS population (Section 3.3). The merger rate assumed in this study is $105.5^{+190.2}_{-83.9} \text{ Gpc}^{-3}\text{yr}^{-1}$ [15]. The detection rate, α , is then the number of signals with SNR above the threshold after the rescaling with respect to the SNR and the time over which we could achieve the desired BNS population.

3.1 Numerical post-merger waveforms

The CoRe Database [42–45] provides a repository of numerical BNS gravitational waveforms for a variety of masses and EOSs. One such waveform is shown in Figure 5. These waveforms are used in this study to calculate the SNRs with a given detector configuration. The total system mass, the individual neutron star masses, peak frequency, and the EOS used to calculate each waveform are recorded. This allows us to investigate the mass distribution inferred from all the available waveforms, the frequency bands of the waveforms, and the change of the peak frequency given a different EOS. It is important to note that to calculate these numerical waveforms, other properties were taken into account, such as the Love number and spin, but these factors were not considered in this study. We do not taken into account the preference of each EOS and treat each waveform in the database with equal probability. However, this equal treatment inevitably causes an artificial preference for frequency ranges of waveforms of certain EOSs, as there is a different number of waveforms for each EOS. As shown in Figure 4, there are far more SLy waveforms than SFHo waveforms, giving SLy waveforms more ‘weight’ than SFHo when calculating α . This weighting may work in our favour given the fact that more established and researched EOSs like SLy are preferenced, but this does not necessarily mean that that particular EOS is more realistic. Better weighting approaches can be investigated in future work.

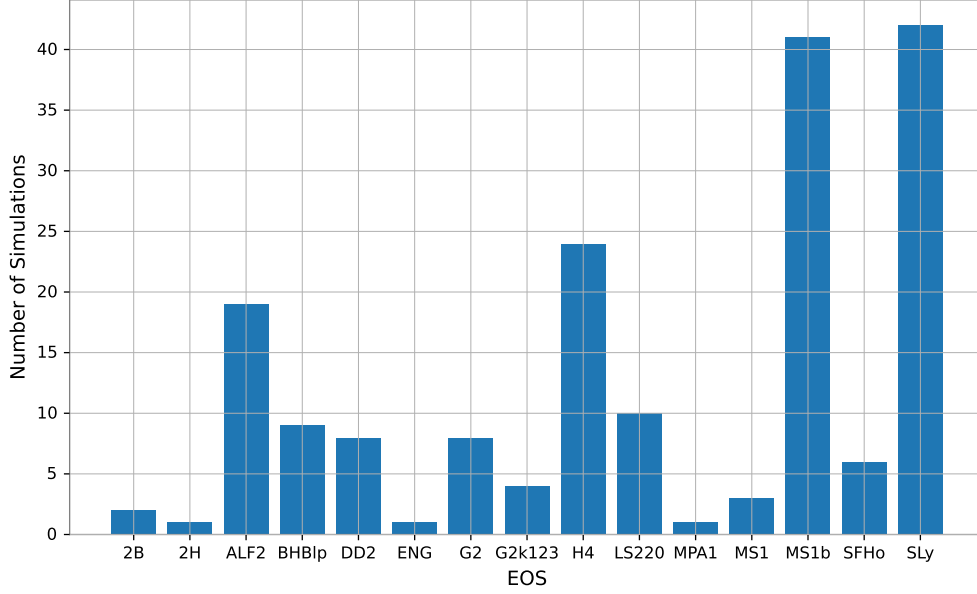


Figure 4: Bar plot of the number of numerical waveforms for each EOS. The x -axis shows the names of the EOS and the y -axis shows the number of waveforms. While some EOS, like MS1b and SLy, have enough waveforms to create a mass distribution similar to the one used in this report, others, like G2, do not.

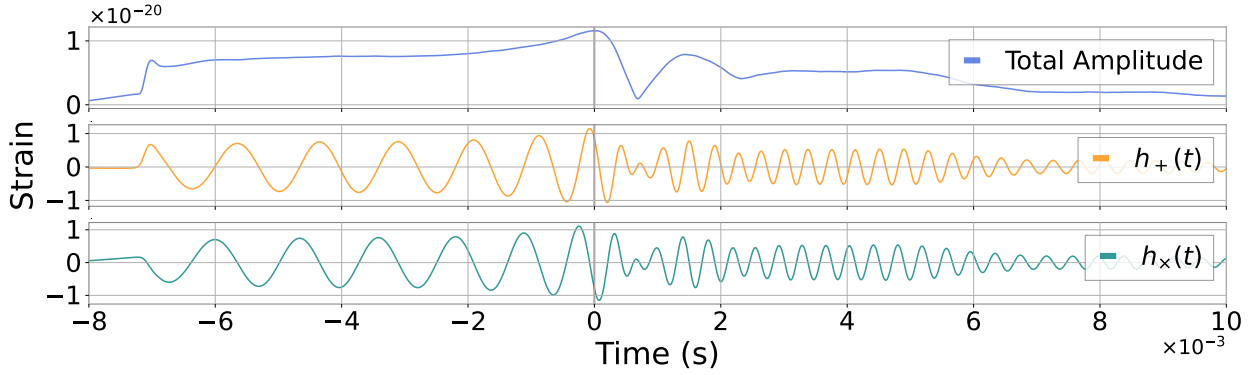


Figure 5: A numerically calculated waveform showing the inspiral, merger, and post-merger signals for a system with total mass $2.7 M_{\odot}$ calculated using the DD2 EOS. The top panel shows the total amplitude of the signal. The middle and bottom panels show the “+” and “ \times ” polarization components of the signal, respectively. The red line indicates the time of the merger, with the post-merger signal occurring to the right. The peak frequency of the signal is given by the frequency at the merger (the time marked by the red line).

The current inferred Galactic BNS mass distributions are given in Figures 2 and 3 in Ref. [46]. Figure 7 shows the mass distribution of all the available numerical waveforms in the database; it has a shape similar to Figure 3 in Ref. [46] (the best Gaussian fit to the Galactic BNS mass distribution) and also has a peak around $1.4 M_{\odot}$. Due to the number of

systems observed in the EM being far larger than the GW, the distributions shown in Figure 7 represent the Galactic population, not the extra-Galactic population. The distributions shown in the Figure for the individual and system mass are also similar, and have peaks around similar values. The mass ratios of the NR waveforms, shown in the third panel, is not similar to that of observed systems. This is reflected in the total system mass distribution being more similar compared to the individual NS masses. This is to be expected as the mass ratios used in simulations are more likely to be ‘normal’ numbers, whereas the observed ratios are heavily dependent on the conditions the system was formed under. The SNR from each numerical waveform will be counted an equal number of times when calculating α . This will then by default represent the mass distribution shown in Figure 7 in the results. There may, however, be a problem with using the Galactic BNS distribution in this study. The mass distribution of neutron stars in gravitational-wave binaries, the extra-Galactic population, is seen to be different with a prevalence in more massive neutron stars [46] giving a double peak. This is unlike the single-peak distributions seen in Figure 7 panel 1. However, we cannot fully confirm the gravitational-wave binary mass distribution as we have yet to observe enough neutron stars in BNS or NSBH systems. This study uses the Galactic mass distribution, but the method can be extended to any given mass distributions.

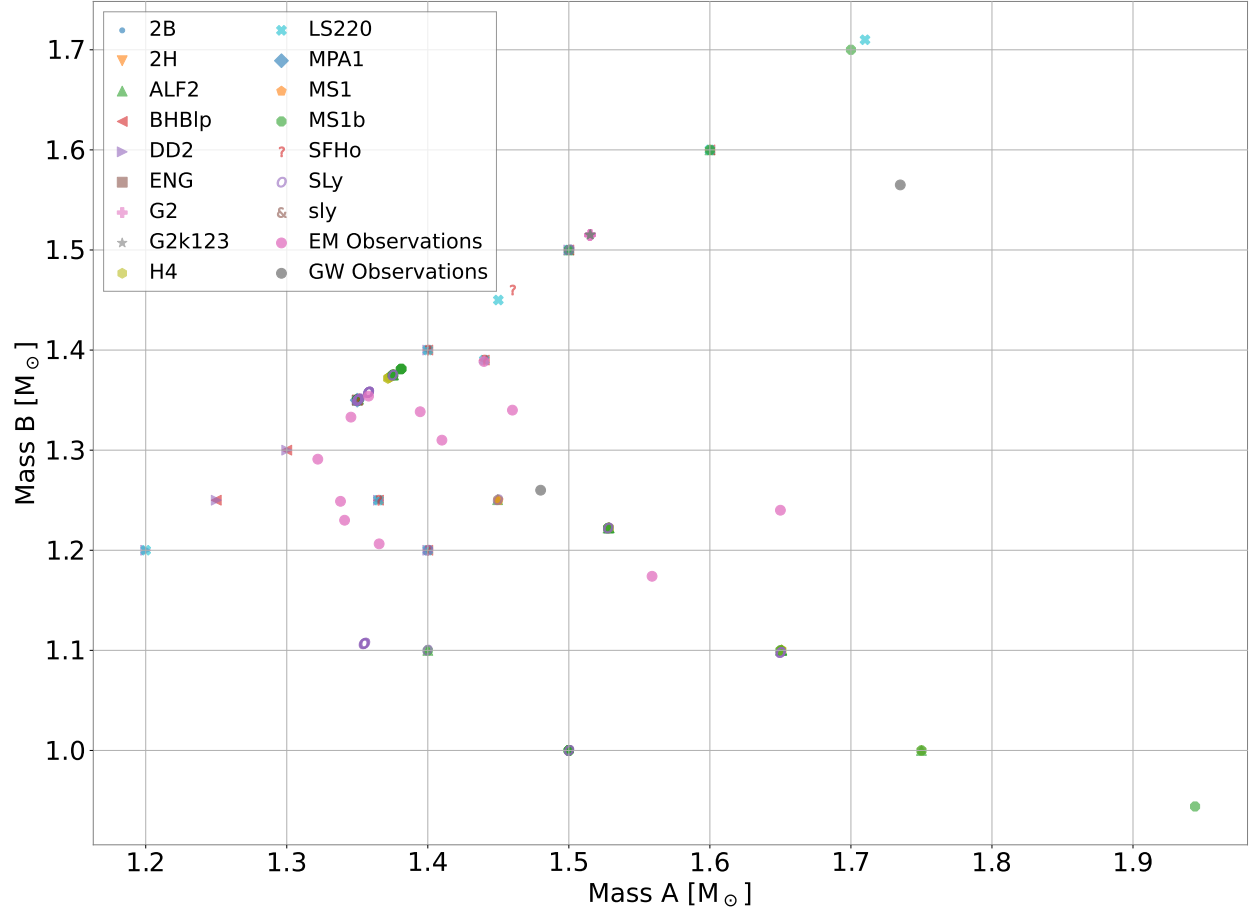


Figure 6: Masses of the individual NSs in the BNSs from the waveforms used in this study and the systems observed in the EM and GW spectra. The x -axis shows the mass of heavier star in M_\odot and the y -axis shows the mass of the lighter star in M_\odot . Note that many mass configurations, for example (1.4,1.4), are repeated in many of the EOS.

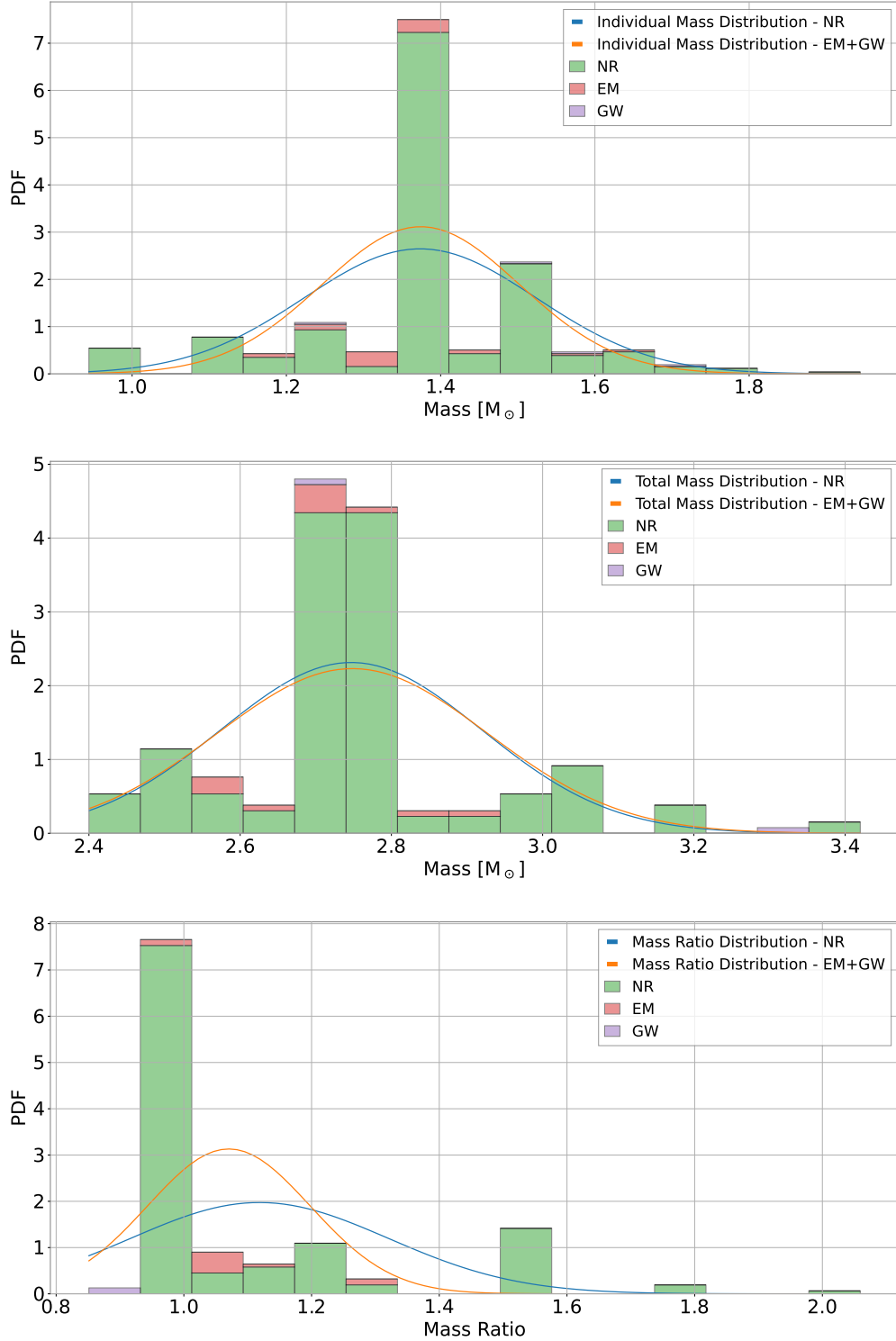


Figure 7: Histograms and distributions of the neutron stars simulated in the numerical waveforms and observed in the EM and GW spectrums in BNSs. Panel 1 and 2 represent the mass distribution for the individual star mass and the total system mass respectively, where x -axis shows the mass in M_{\odot} and the y -axis shows the density. Panel 3 represents the distribution of the ratio of the two masses in the system where the x -axis shows the ratio and the y -axis shows the density. The curves show the Gaussian fit to the discrete data. The curves in panel 1 is similar to the red curve in Figure 3 in Ref. [46] representing the Galactic mass distribution of neutron stars.

3.2 Injections and SNRs

Each of the numerical signal waveforms is injected into a variety of detector configurations at the fiducial distance of 40 Mpc. This is done using the Python package Bilby [25, 47], which uses Bayesian inference to perform parameter estimation. In this study, we use Bilby as a tool to calculate SNRs. Bilby can calculate both ρ_{opt} and ρ_{mf} by inputting a signal and the detector ASD. Note that the SNR is calculated using only the post-merger waveform, as seen in Figure 5 this is the waveform to the right of the red line which indicates the merger. The waveform prior to this line, the inspiral, is not included. The ρ_{opt} and ρ_{mf} outputs were both investigated in order to determine which one to use for calculating α . Note that while ρ_{opt} is constant, ρ_{mf} varies each time it is calculated. As seen in Eqns. (1) and (2), ρ_{mf} is calculated from the strain including randomised noise that varies in each realization, while ρ_{opt} is not impacted by noise realisations. We calculate ρ_{mf} in 300 realisations and compute the mean and the standard deviation. We find that the difference between ρ_{opt} and the mean of ρ_{mf} is consistently less than one standard deviation of the ρ_{mf} distribution. The difference between the two types of SNRs are never greater than one order of magnitude across the detector configurations tested. Considering the fact that the uncertainty caused by noise realisations is far smaller than the uncertainty in the merger rate, using the mean of ρ_{mf} does not improve accuracy but requires more computing power. Thus, for each numerical waveform and detector configuration, we record the ρ_{opt} only.

3.3 Account for populations

The recorded SNRs at this point have the desired mass distribution, but the merger rate and event distribution are not yet taken into account. That is, the distance at which each event is scaled to and the number of events per year are both incorrect. For example, let us assume that the merger systems are uniformly distributed in the Universe (at low redshift) with an event rate of $105.5 \text{ Gpc}^{-3}\text{yr}^{-1}$ [15], and that the maximum detectable range (detector horizon) is 400 Mpc, the number of events occurring in the horizon range per year is roughly 28, not accounting for redshift. However, there are in total 179 waveforms and each needs to be taken into account with an equal number of times to properly represent the mass distribution. To achieve this, we scale the observing time to 6.4 years such that we have 179 events per 6.4 years. After getting a detection rate per 6.4 years, we can rescale that value to get α (per year). By doing so, the desired mass distribution has been properly taken into consideration. Next, we created the distance distribution.

In order to scale the SNR of each event to be consistent with the event distribution at different distances, we need to discretize the distance up to the detector horizon into distance bins and then calculating the number of BNS merger events occurring in that bin. In each bin, the SNRs for the events are scaled to the mean distance of that bin, and the number of events in that bin is also calculated using the mean distance. The sensitivity of a detector naturally decreases as the distance increases and the SNR decreases. The detector horizon is chosen to be the maximum of the horizons across all the configurations. The

detector horizon in this study is set to 400 Mpc, larger than the LIGO-Livingston and LIGO-Hanford BNS detector horizons in O2 when they observed GW170817, which were 218 Mpc and 107 Mpc, respectively [9].

An important parameter in this process is the number and correspondingly the size of the bins if the interval size is kept constant. Decreasing the number of bins will increase the number of events in each bin, but consequently lower the median distances these events are scaled to (because more events happen at larger distances), biasing towards lower distances and inflating the detection rate. Having too few bins thus creates an inaccurate picture of the population. Increasing the number of bins will decrease the number of events in each bin and lead to artifacts in the data due to the small number of samples. This effect is exacerbated as the number of events allocated to each bin needs to be rounded to an integer value. For the detector horizon of 400 Mpc, the number of bins is chosen to be seven. This bin size is chosen by investigating the shape of the histogram created by the discrete distribution. If the detector horizon changes, the number of bins also needs to be changed to produce the most accurate estimation.

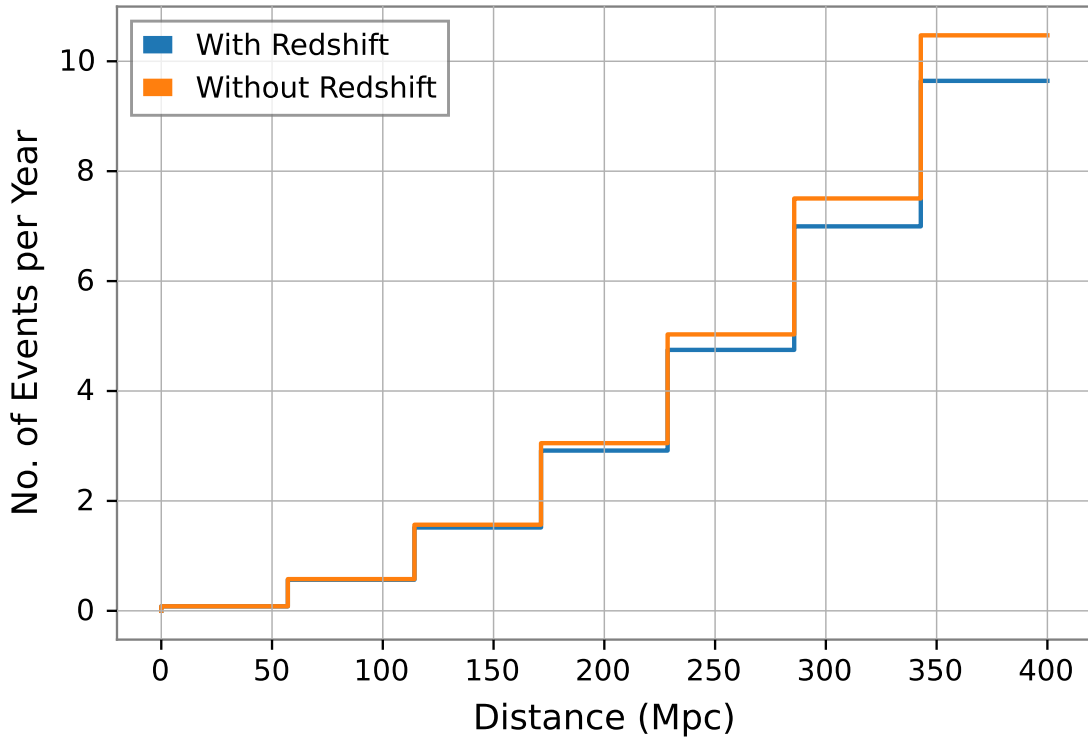


Figure 8: Discrete event distribution with seven bins for an event rate of $105.5 \text{ Gpc}^{-3}\text{yr}^{-1}$ [15]. The x -axis shows the distance in Mpc and the y -axis shows the number of events in each bin. The detector horizon is set to 400 Mpc. The number of events in each bin is calculated with (blue) and without (orange) considering redshift. The difference between the two is negligible, given the fact that redshift at 400 Mpc is on the order of 10^{-2} .

Two methods of calculating the number of events in each bin are used, with and without

considering redshift, as shown in Figure 8. The difference between the two is negligible due to the low redshift at the detector horizon. This difference will become increasingly larger as the detector horizon increases. Regardless, the method that does consider redshift is used in this study. This method calculates a total of 26 merger events in a year occurring in the detector horizon when using an event rate of $105.5 \text{ Gpc}^{-3}\text{yr}^{-1}$ [15], taking into account the redshift. After the number of events in each bin is calculated, the observing time is scaled in order to get a total number of 179 events. The SNR calculated from each waveform is randomly assigned and scaled to the midpoint of a certain distance bin. The number of SNR above the threshold is thus the detection rate per 6.4 years, which can be converted to α . This process is repeated 200 times and an average value is taken for the resulting α . Note that this process implicitly implies that the mass and the distance distribution are not coupled and do not influence each other.

The most recent BNS merger event rate is estimated to be $105.5^{+190.2}_{-83.9} \text{ Gpc}^{-3}\text{yr}^{-1}$ [15]. We take the maximum a posteriori value and the 68% uncertainty boundaries (three values) to calculate α and its uncertainty. The process detailed above is done for each detector configuration for each of the three event rates, and the final result is α with uncertainty for each configuration.

3.4 Optimisation

Calculating α allows for the comparison between different detector configurations; the configuration with the highest α is the most efficient detector. Due to the fact that not all detector configurations are feasible, it is difficult to increase the efficiency by iterating over different physical attributes and maximising α . In practice, we first start with a set of feasible detector configurations. The method detailed in this paper allows for calculating α for a large number of configurations at once. Thus it can potentially infer the preferred regime of multiple physical detector attributes that can result in the most efficient detector.

4 Results

Figure 9 shows α for a variety of NEMO configurations, listed on the x -axis. The α corresponding to the maximum a posteriori value for the estimated event rate is represented by a dot, with the bars indicating the uncertainty up to the 68% confidence interval for the event rate. Evidently, Config_1 (a standard NEMO configuration) is the most efficient one as it has the largest α . At the upper bounds of the uncertainty, this study predicts nearly 2 detectable BNS post-merger signal per decade. Config_14 to Config_20 show an optimisation process where the inner mirror transmission (IMT) and signal recycling mirror transmission (SRMT) were changed in order to shift the most sensitive range towards the 1–4 kHz band where the peak frequency lies for most of the waveforms. Config_14 and Config_16 achieve this to a slightly better degree than the other configurations with

a higher IMT value and a lower SRMT value. These configurations have not been optimised in all the physical attributes of the configuration and many other approaches can be taken to increase α and the efficiency. One such approach is to introduce techniques like quantum squeezing, which is already in effect in Config_1 (thus Config_1 is evidently better). These configurations shown in Figure 9 represent a proof-of-concept for the method detailed in this study.

There is future work to be done to increase the accuracy of the predicted α . The EOS can be investigated further in order to optimise detectors for more physical waveforms. This can be done by removing EOS which are highly unlikely to be physical, or by decreasing the significance of such EOS and increasing the significance of EOS that are more likely to be physical. Being able to predict α from waveforms with similar types of EOS, e.g., only using EOSs with normal nuclear matter in Table 1, would also be interesting. It would allow for more focused investigations into specific configurations that can then be compared. An investigation into the neutron star population by including more gravitational-wave events in the future would also provide a more accurate mass distribution of neutron stars, which directly impacts the results.

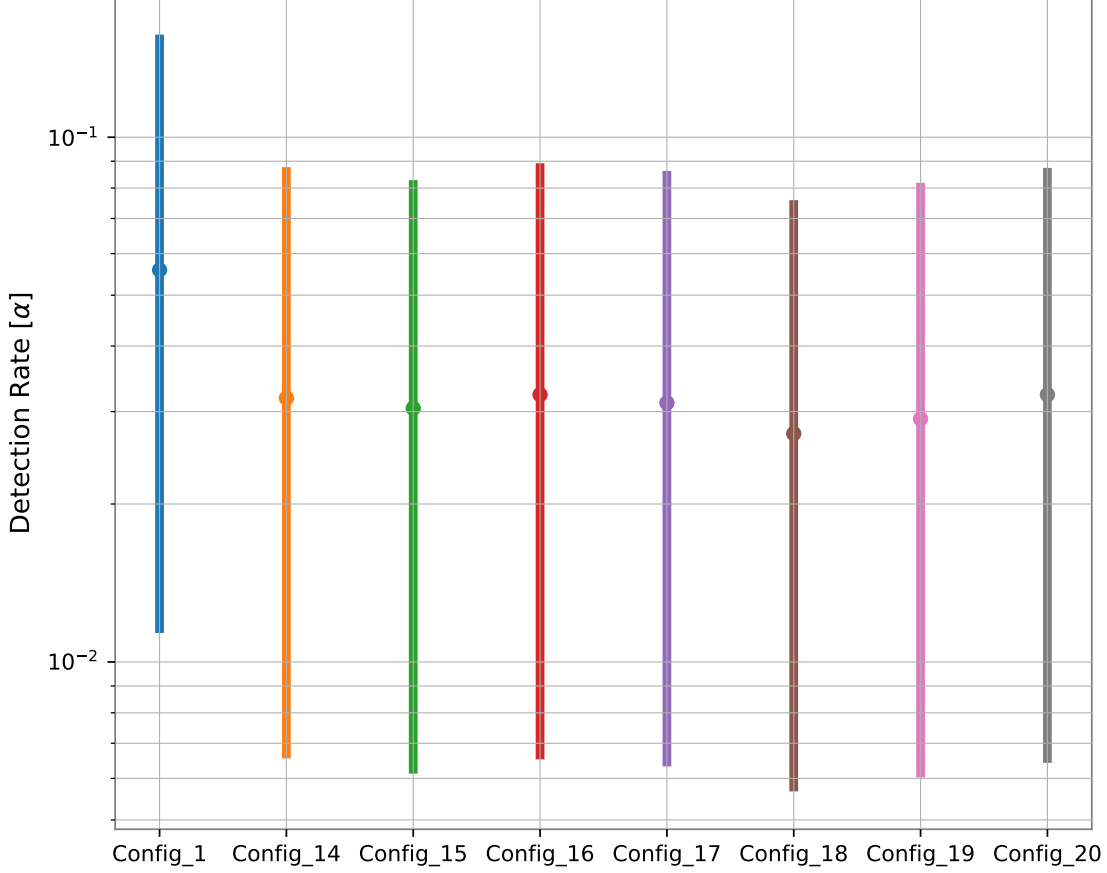


Figure 9: Detection rate per year (α) for a variety of NEMO configurations. The x -axis shows the names of the configurations and the y -axis gives α . The dot represents α corresponding to the maximum a posteriori value for the estimated event rate; the bars indicate the uncertainty bounds of α corresponding to the 68% confidence interval in the estimated event rate. Config_1 is the standard NEMO configuration in Ref. [19]. Note that if we use a binary neutron star merger rate of $250\text{--}2810\text{ Gpc}^{-3}\text{yr}^{-1}$ [10], as used in Ref. [19], the detection rate of the standard NEMO configuration (Config_1) is in the range of $\sim 0.15\text{--}1.5$ events per year. This is consistent with Fig. 5 in Ref. [19] noting that it considers a network of three detectors, and will as a result have a slightly higher detection rate.

5 Conclusion

In this study, we present a method to calculate the detection rate of BNS post-merger signals given a detector configuration. This method uses 165 numerical waveforms from a database as the signal waveforms in order to represent the population of BNS systems with the unknown neutron star EOS. These waveforms, combined with a modelled detector ASD curve, are used to calculate the SNRs of post-merger signals present in the detector, generated by a population of merger systems in the Universe. The number of

SNRs over the detection threshold with any given detector configuration indicates the detection efficiency of the detector. We focus on the main procedure for optimising a NEMO detector in this paper and demonstrate a set of proof-of-concept results. More work needs to be carried out to not only improve the astrophysical assumptions made in this study, e.g., the BNS merger rate and population, existing constraints on EOSs, etc., but to also better investigate feasible detector configurations. This method can be utilised to optimise the NEMO detector for detecting BNS post-merger signals, allowing for groundbreaking discoveries of the physics of extreme matter, gravity and cosmology.

References

- [1] B. S. Sathyaprakash and Bernard F. Schutz. Physics, Astrophysics and Cosmology with Gravitational Waves. *Living Reviews in Relativity*, 12:2, December 2009.
- [2] J. Aasi et al. Advanced LIGO. *Classical and Quantum Gravity*, 32:074001, 2015.
- [3] B. P. Abbott, R. Abbott, T.D. Abbott, and M.R. et. al. Observation of gravitational waves from a binary black hole merger. *Physical Review Letters*, 116(6), feb 2016.
- [4] F. Acernese et al. Advanced Virgo: A second-generation interferometric gravitational wave detector. *Classical and Quantum Gravity*, 32(2):024001, 2015.
- [5] B. P. Abbott et al. Gwtc-1: A gravitational-wave transient catalog of compact binary mergers observed by ligo and virgo during the first and second observing runs. *Phys. Rev. X*, 9:031040, Sep 2019.
- [6] R. Abbott et al. GWTC-2: Compact binary coalescences observed by LIGO and virgo during the first half of the third observing run. *Physical Review X*, 11(2), jun 2021.
- [7] Yoichi Aso, Yuta Michimura, Kentaro Somiya, Masaki Ando, Osamu Miyakawa, Takanori Sekiguchi, Daisuke Tatsumi, and Hiroaki Yamamoto. Interferometer design of the KAGRA gravitational wave detector. *Phys. Rev. D*, 88:043007, Aug 2013.
- [8] R. Abbott et al. Gwtc-3: Compact binary coalescences observed by ligo and virgo during the second part of the third observing run. 2021.
- [9] LIGO Scientific Collaboration and Virgo Collaboration, B.P. Abbott, R. Abbott, T.D. Abbott, F. Acernese, K. Ackley, C. Adams, and T. et al. Adams. GW170817: Observation of Gravitational Waves from a Binary Neutron Star Inspiral. *Physical Review Letters*, 119(16):161101, October 2017. Publisher: American Physical Society.
- [10] B. P. Abbott et al. GW190425: Observation of a compact binary coalescence with total mass $\sim 3.4 m_{\text{sub}\odot}$. *The Astrophysical Journal Letters*, 892(1):L3, mar 2020.
- [11] B. P. Abbott et al. Multi-messenger observations of a binary neutron star merger. *The Astrophysical Journal*, 848(2):L12, oct 2017.

- [12] B. P. Abbott et al. A gravitational-wave standard siren measurement of the Hubble constant. *Nature*, 551(7678):85–88, 2017.
- [13] B P Abbott et al. Model comparison from LIGO–virgo data on GW170817’s binary components and consequences for the merger remnant. *Classical and Quantum Gravity*, 37(4):045006, jan 2020.
- [14] James M. Lattimer. Neutron star equation of state. *New Astronomy Reviews*, 54(3):101–109, March 2010.
- [15] The LIGO Scientific Collaboration, the Virgo Collaboration, the KAGRA Collaboration, R. Abbott, T. D. Abbott, F. Acernese, and K. et al. Ackley. The population of merging compact binaries inferred using gravitational waves through GWTC-3. *arXiv:2111.03634 [astro-ph, physics:gr-qc]*, February 2022. arXiv: 2111.03634.
- [16] B. P. Abbott et al. Search for post-merger gravitational waves from the remnant of the binary neutron star merger GW170817. *The Astrophysical Journal*, 851(1):L16, dec 2017.
- [17] B. P. Abbott et al. Search for gravitational waves from a long-lived remnant of the binary neutron star merger GW170817. *The Astrophysical Journal*, 875(2):160, apr 2019.
- [18] B. P. Abbott et al. Properties of the binary neutron star merger gw170817. *Phys. Rev. X*, 9:011001, Jan 2019.
- [19] K. Ackley, V. B. Adya, P. Agrawal, P. Altin, G. Ashton, M. Bailes, E. Baltinas, A. Barbuio, D. Beniwal, C. Blair, and et al. Neutron star extreme matter observatory: A kilohertz-band gravitational-wave detector in the global network. *Publications of the Astronomical Society of Australia*, 37:e047, 2020.
- [20] Matthew Evans, Rana X Adhikari, Chaitanya Afle, Stefan W. Ballmer, Sylvia Biscoveanu, Ssohrab Borhanian, Duncan A. Brown, Yanbei Chen, Robert Eisenstein, Alexandra Gruson, Anuradha Gupta, Evan D. Hall, Rachael Huxford, Brittany Kamai, Rahul Kashyap, Jeff S. Kissel, Kevin Kuns, Philippe Landry, Amber Lenon, Geoffrey Lovelace, Lee McCuller, Ken K. Y. Ng, Alexander H. Nitz, Jocelyn Read, B. S. Sathyaprakash, David H. Shoemaker, Bram J. J. Slagmolen, Joshua R. Smith, Varun Srivastava, Ling Sun, Salvatore Vitale, and Rainer Weiss. A horizon study for cosmic explorer: Science, observatories, and community. 2021.
- [21] Michele Maggiore et al. Science Case for the Einstein Telescope. *JCAP*, 03:050, 2020.
- [22] J. M. Lattimer and M. Prakash. Neutron Star Structure and the Equation of State. *The Astrophysical Journal*, 550:426–442, March 2001.
- [23] M. C. Miller, F. K. Lamb, A. J. Dittmann, S. Bogdanov, Z. Arzoumanian, K. C. Gendreau, S. Guillot, A. K. Harding, W. C. G. Ho, J. M. Lattimer, R. M. Ludlam, S. Mahmoodifar, S. M. Morsink, P. S. Ray, T. E. Strohmayer, K. S. Wood, T. Enoto, R. Foster, T. Okajima, G. Prigozhin, and Y. Soong. PSR j00300451 mass and radius from

- iNICER/i data and implications for the properties of neutron star matter. *The Astrophysical Journal*, 887(1):L24, dec 2019.
- [24] Andreas Bauswein, Niels-Uwe Friedrich Bastian, David Blaschke, Katerina Chatziioannou, James Alexander Clark, Tobias Fischer, Hans-Thomas Janka, Oliver Just, Micaela Oertel, and Nikolaos Stergioulas. Equation-of-state constraints and the QCD phase transition in the era of gravitational-wave astronomy. In *AIP Conference Proceedings*. AIP Publishing, 2019.
 - [25] Gregory Ashton, Moritz Hübner, Paul D. Lasky, Colm Talbot, Kendall Ackley, Sylvia Biscoveanu, Qi Chu, Atul Divakarla, Paul J. Easter, Boris Goncharov, Francisco Hernandez Vivanco, Jan Harms, Marcus E. Lower, Grant D. Meadors, Denyz Melchor, Ethan Payne, Matthew D. Pitkin, Jade Powell, Nikhil Sarin, Rory J. E. Smith, and Eric Thrane. BILBY: A User-friendly Bayesian Inference Library for Gravitational-wave Astronomy. , 241(2):27, April 2019.
 - [26] Jocelyn S. Read, Benjamin D. Lackey, Benjamin J. Owen, and John L. Friedman. Constraints on a phenomenologically parameterized neutron-star equation of state. December 2008.
 - [27] Thomas E. Riley et al. A NICER view of the massive pulsar PSR j07406620 informed by radio timing and XMM-newton spectroscopy. *The Astrophysical Journal Letters*, 918(2):L27, sep 2021.
 - [28] Horst Müller and Brian D. Serot. Relativistic mean-field theory and the high-density nuclear equation of state. *Nuclear Physics A*, 606(3-4):508–537, sep 1996.
 - [29] Feryal Özel and Paulo Freire. Masses, radii, and the equation of state of neutron stars. *Annual Review of Astronomy and Astrophysics*, 54(1):401–440, 2016.
 - [30] Benjamin Lackey. The Neutron-Star Equation of State and Gravitational Waves from Compact Binaries. *Theses and Dissertations*, August 2012.
 - [31] E. Chabanat, P. Bonche, P. Haensel, J. Meyer, and R. Schaeffer. A skyrme parametrization from subnuclear to neutron star densities part ii. nuclei far from stabilities. *Nuclear Physics A*, 635(1):231–256, 1998.
 - [32] Benjamin D. Lackey, Mohit Nayyar, and Benjamin J. Owen. Observational constraints on hyperons in neutron stars. *Physical Review D*, 73(2), jan 2006.
 - [33] Mark Alford, Matt Braby, Mark Paris, and Sanjay Reddy. Hybrid stars that masquerade as neutron stars. *The Astrophysical Journal*, 629(2):969–978, aug 2005.
 - [34] Tobias Fischer, Matthias Hempel, Irina Sagert, Yudai Suwa, and Jürgen Schaffner-Bielich. Symmetry energy impact in simulations of core-collapse supernovae. *The European Physical Journal A*, 50(2), feb 2014.

- [35] Kuo-Chuan Pan, Matthias Liebendörfer, Sean M. Couch, and Friedrich-Karl Thielemann. Equation of state dependent dynamics and multi-messenger signals from stellar-mass black hole formation. *The Astrophysical Journal*, 857(1):13, apr 2018.
- [36] Sarmistha Banik, Matthias Hempel, and Debades Bandyopadhyay. NEW HYPERON EQUATIONS OF STATE FOR SUPERNOVAE AND NEUTRON STARS IN DENSITY-DEPENDENT HADRON FIELD THEORY. *The Astrophysical Journal Supplement Series*, 214(2):22, sep 2014.
- [37] Jocelyn S. Read, Charalampos Markakis, Masaru Shibata, Kōji Uryū, Jolien D. E. Creighton, and John L. Friedman. Measuring the neutron star equation of state with gravitational wave observations. *Physical Review D*, 79(12), jun 2009.
- [38] L. Engvik, M. Hjorth-Jensen, E. Osnes, G. Bao, and E. Østgaard. Asymmetric nuclear matter and neutron star properties. *Physical Review Letters*, 73(20):2650–2653, nov 1994.
- [39] Chencan Wang, Jinniu Hu, Ying Zhang, and Hong Shen. The nuclear symmetry energy from relativistic brueckner-hartree-fock model *. *Chinese Physics C*, 46(6) : 064108, jun 2022.
- [40] Bernard F Schutz. Networks of gravitational wave detectors and three figures of merit. *Classical and Quantum Gravity*, 28(12):125023, may 2011.
- [41] Paul D. Lasky, Eric Thrane, Yuri Levin, Jonathan Blackman, and Yanbei Chen. Detecting gravitational-wave memory with LIGO: Implications of GW150914. *Physical Review Letters*, 117(6), aug 2016.
- [42] Computational Relativity.
- [43] Tim Dietrich, David Radice, Sebastiano Bernuzzi, Francesco Zappa, Albino Perego, Bernd Bruegmann, Swami Vivekanandji Chaurasia, Reetika Dudi, Wolfgang Tichy, and Maximiliano Ujevic. CoRe database of binary neutron star merger waveforms and its application in waveform development. *arXiv:1806.01625 [astro-ph, physics:gr-qc]*, June 2018.
- [44] Reetika Dudi, Francesco Pannarale, Tim Dietrich, Mark Hannam, Sebastiano Bernuzzi, Frank Ohme, and Bernd Bruegmann. Relevance of tidal effects and post-merger dynamics for binary neutron star parameter estimation. *Physical Review D*, 98(8):084061, October 2018.
- [45] Alessandro Nagar, Sebastiano Bernuzzi, Walter Del Pozzo, Gunnar Riemenschneider, Sarp Akcay, Gregorio Carullo, Philipp Fleig, Stanislav Babak, Ka Wa Tsang, Marta Colleoni, Francesco Messina, Geraint Pratten, David Radice, Piero Retteno, Michalis Agathos, Edward Fauchon-Jones, Mark Hannam, Sascha Husa, Tim Dietrich, Pablo Cerda-Duran, Jose A. Font, Francesco Pannarale, Patricia Schmidt, and Thibault Damour. Time-domain effective-one-body gravitational waveforms for coalescing compact binaries with nonprecessing spins, tides and self-spin effects. *Physical Review D*, 98(10):104052, November 2018.

- [46] Philippe Landry and Jocelyn S. Read. The Mass Distribution of Neutron Stars in Gravitational-wave Binaries. *The Astrophysical Journal Letters*, 921(2):L25, November 2021.
- [47] I. M. Romero-Shaw, C. Talbot, et al. Bayesian inference for compact binary coalescences with BILBY: validation and application to the first LIGO-Virgo gravitational-wave transient catalogue. , 499(3):3295–3319, December 2020.